Earth and Planetary Science Letters 621 (2023) 118354

Contents lists available at ScienceDirect

Earth and Planetary Science Letters

journal homepage: www.elsevier.com/locate/epsl

Erosion rate maps highlight spatio-temporal patterns of uplift and quantify sediment export of the Northern Andes

Richard F. Ott [a,b,*], Nicolás Pérez-Consuegra [c,d], Dirk Scherler [a,e], Andrés Mora [f], Kimberly L. Huppert [b,g], Jean Braun [b], Gregory D. Hoke [h], Jose R. Sandoval Ruiz [i]

[a] Earth Surface Geochemistry, GFZ German Centre for Geoscience Research, Potsdam, Germany
[b] Earth Surface Process Modelling, GFZ German Centre for Geoscience Research, Potsdam, Germany
[c] Department of Earth, Atmospheric and Planetary Sciences, Massachusetts Institute of Technology, Cambridge, USA
[d] Department of Earth and Environmental Sciences, Weber State University, Ogden, UT, USA
[e] Institute of Geographical Sciences, Freie Universität Berlin, Berlin, Germany
[f] Ecopetrol, Rio de Janeiro, Brazil
[g] Department of Earth and Atmospheric Science, City College of New York, New York, USA
[h] Department of Earth and Environmental Sciences, Syracuse University, Syracuse, USA
[i] Instituto Colombiano del Petróleo – ICP, Ecopetrol S.A, Piedecuesta, Colombia

ARTICLE INFO

Article history:
Received 20 February 2023
Received in revised form 11 June 2023
Accepted 11 August 2023
Available online 15 September 2023
Editor: J.P. Avouac

Dataset link:
doi.org/10.5281/ZENODO.8021046

Keywords:
Colombia
cosmogenic nuclides
subduction geometry
steady-state topography
Eastern Cordillera
Central Cordillera

ABSTRACT

Erosion rates are widely used to assess tectonic uplift and sediment export from mountain ranges. However, the scarcity of erosion rate measurements often hinders detailed tectonic interpretations. Here, we present 25 new cosmogenic nuclide-derived erosion rates from the Northern Andes of Colombia to study spatio-temporal patterns of uplift along the Central and Eastern Cordillera. Specifically, we combine new and published erosion rate data with precipitation-corrected normalized channel steepness measurements to construct high-resolution erosion rate maps. We find that erosion rates in the southern Central Cordillera are relatively uniform and average ~0.3 mm/a. In the northern Central Cordillera rapidly eroding canyons dissect slowly eroding, low-relief surfaces uplifting since $8.3^{+3.7}_{-2.6}$ Ma, based on a block uplift model. We interpret that persistent steep slab subduction has led to an erosional steady-state in the southern Central Cordillera, whereas in the northern Central Cordillera, Late Miocene slab flattening caused an acceleration in uplift, to which the landscape has not yet equilibrated. The Eastern Cordillera also displays pronounced erosional disequilibrium, with a slowly eroding central plateau rimmed by faster eroding western and eastern flanks. Our maps suggest Late Miocene topographic growth of the Eastern Cordillera, with deformation focused along the eastern flank, which is also supported by balanced cross-sections and thermochronologic data. Spatial gradients in predicted erosion rates along the eastern flank of the Eastern Cordillera suggest transient basin-ward migration of thrusts. Finally, sediment fluxes based on our erosion maps, suggest that the Eastern Cordillera exports nearly four times more sediment than the Central Cordillera. Our analysis shows that accounting for spatial variations in erosion parameters and climate reveals important variations in tectonic forcing that would otherwise be obscured in traditional river profile analyses. Moreover, given relationships between tectonic and topographic evolution, we hypothesize that spatio-temporal variations in slab dip are the primary driver of the dynamic landscape evolution of the Northern Andes, with potentially superposed effects from inherited Mesozoic rift structures.

1. Introduction

Erosion plays a major role in controlling the large-scale topography and tectonics of mountain ranges (Beaumont et al., 1992; Wolf et al., 2022). In most mountain ranges on Earth, rivers are the key erosion agents. Rivers generate relief by incision and they also transport sediment to adjacent sedimentary basins, influencing basin evolution and providing nutrients vital to ecosystem productivity (Hoorn et al., 2010). Where rivers are subjected to constant climatic and tectonic forcing for sufficient periods of time, they tend to adjust their slopes so that erosion rates everywhere approximately balance rock uplift rates (Kirby and Whipple,

* Corresponding author at: Telegrafenberg, 14473 Potsdam, Germany.
E-mail address: richard.ott1900@gmail.com (R.F. Ott).

https://doi.org/10.1016/j.epsl.2023.118354

2012). In such topographic steady-state, variations in the normalized steepness of river reaches (river slope normalized for drainage area) arise locally from variations in rock uplift rate (≈ erosion rate), erosional parameters (e.g., bedrock erodibility), and climate (Howard, 1994). Conversely, temporal changes in climate or rock uplift rates generate disequilibrium landscapes, where different regions erode at different rates, separated by transient changes in normalized river steepness that travel upstream (Kirby and Whipple, 2012). The time-scale of landscape adjustment to new forcing depends on the erosional parameters, precipitation, and river slope, and is typically on the order of millions of years (Whipple et al., 2017). Because the response of a landscape to a temporal change in uplift rate follows a predictable pattern, spatial variations in normalized river steepness can be used to infer not only spatial but also temporal variations in erosion and rock uplift rates, provided erosional parameters can be constrained (Schildgen et al., 2012).

Direct measurements of erosion rates from a subset of catchments across a landscape make it possible to constrain erosional parameters and thereby decipher spatio-temporal patterns in uplift from variations in normalized channel steepness. Specifically, cosmogenic radionuclides (CRNs) measured in river sediments are commonly used to determine millennial, catchment-averaged erosion rates (Granger et al., 1996), which should equal rock uplift rates in steady-state landscapes (Kirby and Whipple, 2012). However, over large spatial scales or in transiently adjusting regions, inferring uplift rates from CRN-derived erosion rates is a tedious endeavor that requires large data sets. To circumvent this issue, CRN-derived erosion rates from well-adjusted portions of the landscape can be used to constrain the relationship between normalized channel steepness and erosion rate (Ouimet et al., 2009), which can then be used to infer erosion rates from normalized channel steepness maps elsewhere (Adams et al., 2020). These erosion rate maps offer the potential to examine spatial and temporal patterns of erosion and rock uplift in regions with complex tectonics and climate, such as the Northern Andes (Fig. 1).

Several open questions exist regarding the timing and spatial patterns of rock and surface uplift in the two main mountain ranges of the Northern Andes; the Central Cordillera (CC), a mountain range composed of crystalline basement rocks and dotted with the modern volcanic arc, and the Eastern Cordillera (EC), a doubly verging sedimentary fold and thrust belt. In the CC, it remains unclear if along-strike differences in erosion exist (Villagómez and Spikings, 2013), and whether orogenic growth mostly pre-dates the Late Miocene (Restrepo-Moreno et al., 2009, 2019), or if the northern CC has been uplifted only subsequently (Pérez-Consuegra et al., 2021b). Surface uplift of the EC established a new orographic barrier that had major effects on biodiversity by disrupting east-draining river (Rodriguez-Muñoz et al., 2022). However, it remains debated if elevations comparable to modern were achieved in Oligocene to mid-Miocene times (Anderson et al., 2015; Mora-Páez et al., 2016; Rodriguez-Muñoz et al., 2022) or whether the main surface uplift occurred since the Late Miocene (Hooghiemstra et al., 2006; Mora et al., 2008), as well as how erosion rates vary along the orogen flanks (Struth et al., 2017). We propose that erosion rate maps could elucidate patterns of rock uplift through space and time, when coupled with landscape evolution predictions, to differentiate between hypotheses of surface uplift timing and patterns of erosion rates within the CC and EC.

Here we present 25 new CRN-derived erosion rates from the CC, which we combine with published CRN data from the EC to quantify erosion as a function of bedrock-related erosional parameters, climate, and normalized channel steepness. We developed an optimization algorithm to extrapolate our new and existing measurements and infer erosion rates from the normalized steepness of river channels at 30-m resolution for the Northern Andes. We then use these inferred erosion rate maps to interpret patterns of tectonic rock uplift in space and time and predict sediment fluxes to neighboring sedimentary basins. These analyses highlight the influence of subduction dynamics on the evolution of the CC and EC and quantify sediment export to the Andean foreland.

2. Study area

The Northern Andes are formed by subduction of the Nazca and Caribbean plates beneath the South American Plate (Taboada et al., 2000). South of 5-6° N, the Nazca Plate subducts steeply below the South American Plate at a rate of ∼ 50 mm/a (Trenkamp et al., 2002). Flat slab subduction occurs north of 5-6°N since about 6-8 Ma (Wagner et al., 2017) (Fig. 1A). It remains unclear debated whether the slab imaged north of 5-6° belongs to a previously continuous Nazca slab that tore (Wagner et al., 2017), or whether there is overlap between the Caribbean and Nazca slabs (Sun et al., 2022).

On the surface, the Northern Andes manifest as three parallel, roughly north-south striking mountain ranges: the Western, Central, and Eastern Cordillera (WC, CC, EC). The CC and EC are separated by the intermontane Magdalena Valley (Fig. 1). The CC is primarily composed of Paleozoic (meta-)granitoids, Triassic metasediments and meta-intrusive rocks, and extensive Jurassic and Cretaceous batholiths (Villagómez et al., 2011). South of 5°N, Plio-Quaternary volcanic rocks from active arc volcanism outcrop in several locations near the crest of the CC. The EC is an inverted Mesozoic rift structure that has turned into a doubly-verging fold-and-thrust belt (Cooper et al., 1995). The bedrock of the EC is mostly Mesozoic quartzose sandstones and mudstones, with some minor occurrences of Cenozoic and Paleozoic clastic sedimentary rocks and crystalline basement (Cooper et al., 1995).

The topographic evolution of the CC and EC is debated. Sedimentary and thermochronological records suggest that the CC existed throughout the Cenozoic and potentially Cretaceous (Gómez et al., 2005; Villagómez and Spikings, 2013). However, it remains debated if the northern CC rose to high elevations (> 2000 m) by about 25 Ma (Restrepo-Moreno et al., 2019) or only within the past 5 Ma due to recent slab flattening (Pérez-Consuegra et al., 2021b). For the EC, pollen and some thermochronological studies suggest that most of the surface uplift and exhumation occurred since the Late Miocene (e.g., Hooghiemstra et al., 2006; Anderson et al., 2016), while others argue that elevations close to modern were achieved in the Oligocene to mid-Miocene (Anderson et al., 2015; Mora-Páez et al., 2016; Rodriguez-Muñoz et al., 2022). What drives mountain building in the EC remains debated; some studies argue that crustal thickening controlled by inherited Mesozoic rift structures controls rock and surface uplift (Mora et al., 2006, 2013), while others suggest that slab flattening drove changes in dynamic topography and Neogene uplift (Siravo et al., 2019).

3. Methods

3.1. Cosmogenic ^{10}Be measurements

We collected 25 river sediment samples along the CC to measure in-situ ^{10}Be-derived catchment-average erosion rates. In the northern CC, most streams exhibit major knickpoints. Our aim was to focus on steady-state channel reaches; therefore, we sampled basins that were either entirely below or above major knickpoints. For details about the chemical separation and the erosion rate calculation, please see the supplemental text.

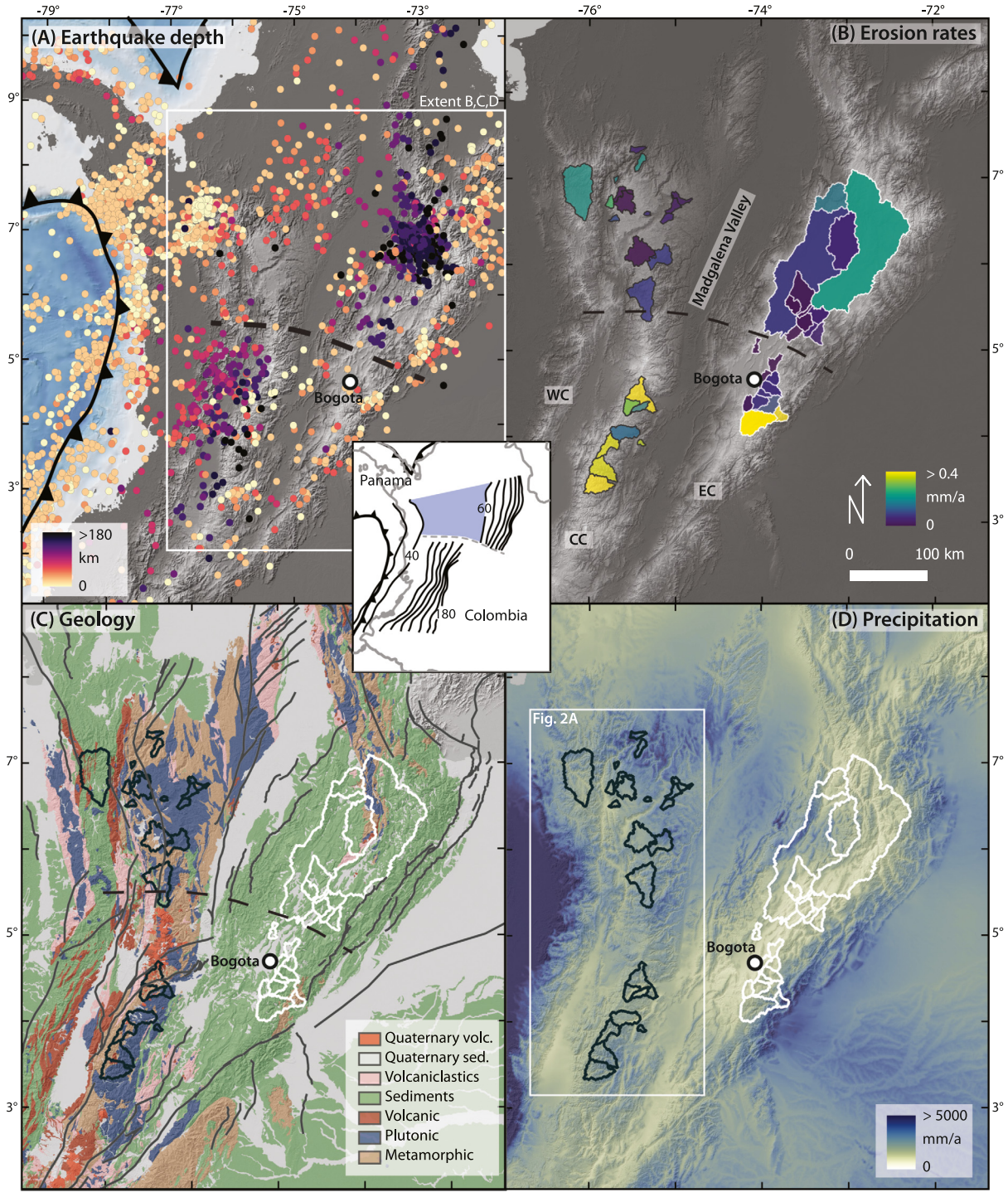

Fig. 1. Overview of the study area and CRN sampling locations. (*A*) Regional subduction zones and earthquake hypocenter depths (> M_w 4) (U.S. Geological Survey, 2020). Inset: slab depth in the study area at 20-km contour intervals (Wagner et al., 2017) with a dashed line representing the location of the proposed slab tear. Blue shading indicates the region of flat slab subduction. (*B*) Catchment-average erosion rates in the CC and WC from this study (black outlines) and samples recalculated from Struth et al. (2017) in the EC (white outlines). (*C*) Simplified geologic map showing the lithology of the analyzed basins based on Gomez and Montes (2020) and active faults from Veloza et al. (2012). For the CC, all basins lie within plutonic and metamorphic catchments. The basins within the EC are almost exclusively within clastic sedimentary rocks. (*D*) Mean annual precipitation saturated at 5000 mm/a. White box highlights the location of Fig. 2A.

3.2. Topographic analysis

3.2.1. Stream power incision model

To predict erosion rates in the Northern Andes, we build on the stream power incision model (SPIM) for detachment-limited rivers (Howard, 1994), which predicts the erosion of a riverbed as

$$E = K * A^m * S^n, \quad (1)$$

where channel bed elevations are lowered by river incision E, which is a function of the upstream drainage area A, channel slope S, and the dimensional erodibility coefficient K. Exponents m and n are empirical constants related to the incision process, basin hydrology, and channel geometry (Whipple et al., 2000). The

SPIM includes several simplifying assumptions such as a uniform power-law scaling between channel width and discharge and a negligible effect of channel sediment variations on the incision or shielding the channel bed (see Whipple and Tucker, 1999 for more information). This equation can be rearranged to show the commonly observed power-law scaling between local channel slope and drainage area (Flint, 1974)

$$S = k_s * A^{-\theta}, \tag{2}$$

with

$$k_s = \left(\frac{E}{K}\right)^{\frac{1}{n}} \text{ and} \tag{3}$$

$$\theta = \frac{m}{n}. \tag{4}$$

Channel steepness, k_s, is the channel slope normalized for the downstream increase in drainage area and concavity of the channel, θ, and is predicted to have a direct relationship with incision rate. To compare the k_s among multiple streams, a reference concavity θ_{ref} must be determined, which results in the normalized channel steepness k_{sn} (Wobus et al., 2006).

3.2.2. k_{sn} calculation

To minimize the impact of varying erodibility K, we targeted catchments dominated by granites and gneisses, with a few basins containing some metamorphic mica schists. Sampling steady-state basins with homogeneous lithology enabled us to use the ^{10}Be-derived erosion rates to define the stream power parameters n and K by rearranging Eq. (3):

$$E = K * {k_{sn}}^n. \tag{5}$$

We measured k_{sn} using TopoToolbox (TT) (Schwanghart and Scherler, 2014) and the 30-m Copernicus Digital Elevation Model (DEM). Specifically, we calculated mean basin k_{sn} for all sampled basins using χ-elevation regressions (TT 'chiplot' function). We employed a Bayesian optimization that linearizes stream profiles to constrain the reference concavity θ_{ref} (TT 'mnoptim'). The concavity optimization was performed on the southern CC where stream-profiles are near equilibrium (Pérez-Consuegra et al., 2021b) to avoid a biased concavity estimate from transient profiles in the northern CC. This yielded a $\theta_{ref} = 0.5$ (Fig. S1). To estimate θ_{ref} for the EC, the Altiplano surface was removed from the DEM, resulting in a best-fit concavity value of 0.45 (Fig. S1). We smoothed river bed elevations using constrained regularized smoothing (TT-function 'crs') with a tau value (elevation quantile) of 0.25 to account for positive DEM errors in valley bottoms (Schwanghart and Scherler, 2017) and a smoothing value of 10. To calculate k_{sn}, we used a critical drainage area for stream initiation of 5 km^2, based on our observations of a systematic drop in k_{sn} at lower drainage areas with the smoothing parameters applied (Fig. S2).

In Eq. (1), drainage area serves as a proxy for stream discharge. However, precipitation varies across the study area, which could change the discharge-drainage area scaling and potentially bias $k_{sn} - E$ comparisons. To address this, we used a precipitation-corrected channel steepness k_{sn-P} equivalent to k_{sn-q} defined by Adams et al. (2020), where

$$k_{sn-P} = (A * P)^{\theta_{ref}} * S \tag{6}$$

with P referring to the upstream-averaged mean annual precipitation. For calculation, we used the 500-m resolution CHELSA mean annual precipitation grid (Karger et al., 2017) as weighting for the flow accumulation algorithm. To illustrate how our results would differ without this correction, we also show results based on k_{sn}.

3.2.3. Inferred erosion rate maps

Provided that n and K are known and are considered to be constant within each mountain range, Eq. (5) makes it possible to convert a k_{sn-P} map to an inferred erosion rate map. To do this, k_{sn-P} values were projected from streams onto the hillslopes by reversing the flow routing, ensuring that no smoothing occurs across drainage divides (TT-function 'mapfromnal'). Eq. (5) was used together with n and K to convert k_{sn-P} to erosion rates. For further details, we refer the reader to the Matlab example script in Ott (2023). Projecting river incision values onto the hillslopes assumes that incision and hillslope erosion are coupled, which is an implicit assumption of all studies comparing k_{sn} to cosmogenic nuclide-derived erosion rates (e.g., DiBiase et al., 2010; Adams et al., 2020). Previous studies with high-resolution topographic data have shown a strong coupling between channels and hillslopes across large gradients of uplift rate (Hurst et al., 2019), despite potential time lags in areas of recent uplift rate change (Clubb et al., 2020). Based on the range of mean k_{sn-P} of CRN-sampled catchments in the CC and EC, in both cases about 75% of the erosion rate map is interpolated between measured erosion rate data and 25% are extrapolated.

To determine the best fit n and K parameters for the inferred erosion map, we developed an optimization algorithm that minimizes the misfit between measured and predicted erosion rates in the two cordilleras separately. We tested a range of reasonable n (0.5 to 4.5) and K (10^{-14} to 10^{-6}) values. For every parameter combination, we calculated an inferred erosion rate map and used it to predict erosion rates for each sampling location by taking the average of all upstream pixel values. Subsequently, a weighted

$$\phi_w = \frac{1}{n_s} \sum_i \left(\frac{E - E_m}{dE}\right)^2 \tag{7}$$

and non-weighted misfit function

$$\phi = \frac{1}{n_s} \sum_i (E - E_m)^2, \tag{8}$$

are computed to define the best-fit models, where E_m refers to the modeled erosion rate for each sample i, dE to its reported erosion rate uncertainty, and n_s to the total number of samples. We apply two different misfit functions to investigate the effect of uneven erosion rate distribution on the optimization parameters. To limit the variability in K, we estimate erosion rates in the CC only within areas underlain by crystalline basement rocks, including minor Quaternary volcanic exposures. Similarly, in the EC, we only estimate erosion rates within areas predominantly covered by siliciclastic sediments. Commonly, power law regressions of k_{sn} or k_{sn-P} and erosion rate data are used to determine the values of K and n (Hilley et al., 2019; Adams et al., 2020). However, our approach has several advantages over using standard power law regressions, which we discuss in section 5.3.

4. Results

4.1. Erosion rates

Our 25 new CRN-derived erosion rates sample different geomorphic subregions of the CC (Fig. 2). Pérez-Consuegra et al. (2021b) showed that the southern CC comprises high relief topography (Fig. 2C) with steep river profiles whereas, in the northern CC, steep rivers dissect a series of low-relief plateau surfaces (Antioqueno Plateau) rimmed by knickpoints. Overall, the low-relief, high-elevation surfaces of the northern CC are flat in the west. In the east, they gently slope down towards the Magdalena River (Fig. 2B). Therefore, we separate the erosion rates from the CC

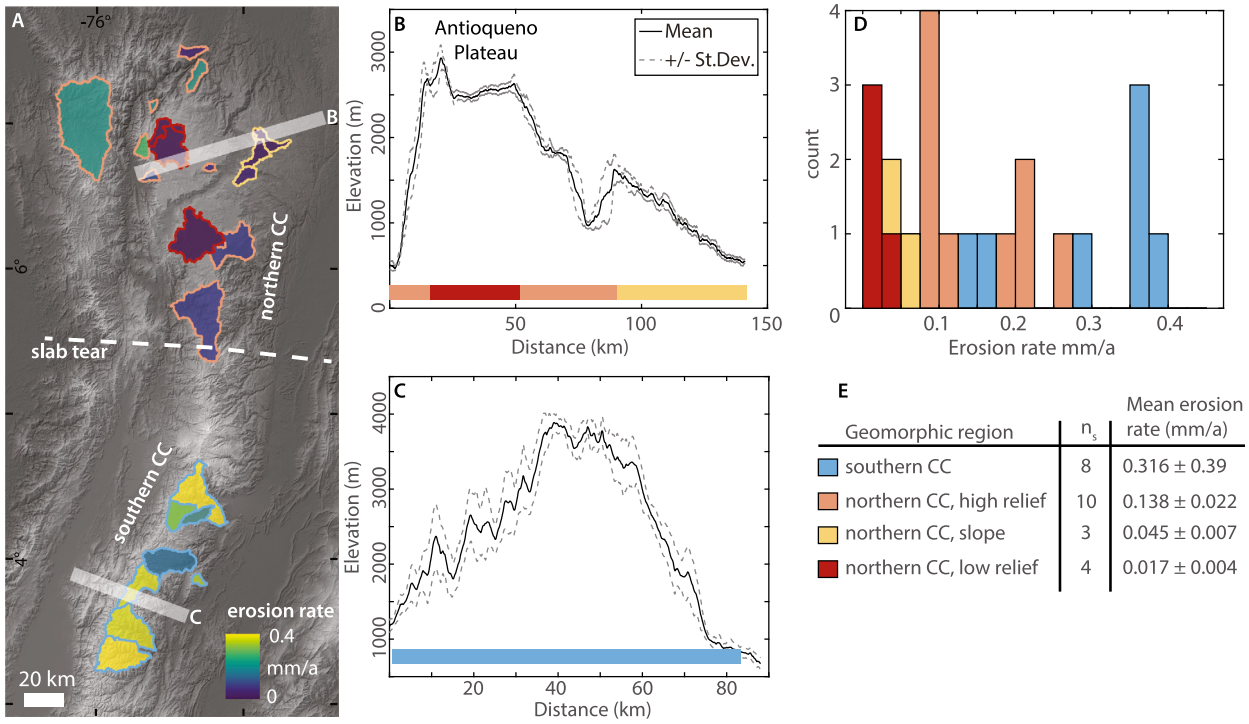

Fig. 2. (*A*) Catchment average erosion rates of the CC with approximate location of the slab tear at depth (for location see Fig. 1D). The catchment outlines are colored by geomorphic region with the color code shown in (*E*). (*B*) and (*C*) swath profiles across the northern and southern CC, respectively. Swath locations are shown in (*A*). Colors indicate different geomorphic domains. Note the low standard deviation of elevation in the northern CC highlighting the low-relief surfaces. (*D*) Erosion rate histogram grouped by geomorphic region. (*E*) Mean erosion rates for the geomorphic regions, were computed by drawing normally distributed erosion rates based on the erosion rate uncertainties and calculating the mean for 5000 bootstrap samples. The mean and standard deviation were determined from the bootstrap sampling distribution.

Table 1
AMS data and erosion rates from the CC.

Sample	AMS code	Lat (°)	Lon (°)	Catchment area (km^2)	$^{10}Be/^{9}Be$	Error (%)	^{9}Be carrier[a] (mg)	Quartz weight (g)	^{10}Be[b] (at/g)	Production rate (at/g/a)	Erosion rate (mm/a)
CC21-02	s17764	3.9061	−75.3408	39.1	8.53e-14	4.76	0.2045	45.4528	18900 ± 1000	9.13	0.351 ± 0.032
CC21-03	s17765	3.4711	−75.6655	651.4	1.61e-13	4.35	0.2024	46.4912	35700 ± 1600	18.36	0.362 ± 0.033
CC21-04	s18013	3.4256	−75.6967	653.6	1.3Ee-13	4.83	0.2118	41.9136	33400 ± 1700	18.70	0.394 ± 0.037
CC21-05	s17766	3.8514	−75.6588	393.9	1.91e-13	4.23	0.2030	47.8881	41700 ± 1800	21.27	0.358 ± 0.032
CC21-14	s18014	4.0548	−75.4099	546.7	2.98e-13	3.54	0.2127	41.0355	80500 ± 2900	16.32	0.142 ± 0.012
CC21-15	s18015	4.2979	−75.2049	1041.1	7.80e-14	5.07	0.2133	35.202	23200 ± 1300	15.38	0.469 ± 0.045
CC21-16	s18016	4.4003	−75.2930	161.8	2.43e-13	3.71	0.2129	45.4415	59000 ± 2300	14.16	0.169 ± 0.015
CC21-17	s17767	4.4060	−75.4320	260.3	1.94e-13	4.22	0.2028	45.344	44600 ± 2000	17.97	0.284 ± 0.025
CC21-18	s17768	5.9992	−75.0684	543.9	3.65e-13	3.68	0.2016	49.9427	77000 ± 2900	9.42	0.087 ± 0.007
CC21-19	s18017	6.0733	−75.2279	17.8	3.61e-13	3.70	0.2129	44.022	91200 ± 3400	11.39	0.088 ± 0.008
CC21-20	s17769	6.2347	−75.3242	808.5	1.82e-12	3.26	0.2026	48.6489	402000 ± 13200	11.92	0.02 ± 0.002
CC21-21	s17770	6.5819	−75.5113	490.5	2.93e-12	3.23	0.2021	49.2343	636500 ± 20600	15.24	0.016 ± 0.001
CC21-22	s18018	6.8519	−75.4881	44.3	5.46e-12	3.06	0.2128	42.989	1435300 ± 44000	16.07	0.007 ± 0.001
CC21-23	s18019	6.5712	−75.2809	35.9	3.68e-13	3.87	0.2131	44.057	93100 ± 3700	10.82	0.082 ± 0.007
CC21-24	s17771	6.6611	−74.9254	181.5	5.31e-13	3.48	0.2015	48.7424	115200 ± 4100	6.97	0.044 ± 0.004
CC21-25	s18020	6.7638	−74.8024	161.4	5.07e-13	3.31	0.2129	37.671	150500 ± 5100	6.65	0.032 ± 0.003
CC21-26	s17772	6.5394	−75.0252	135.1	4.20e-13	3.62	0.2006	49.2864	89500 ± 3300	7.48	0.06 ± 0.005
ANT18-01	s18022	5.7128	−75.5406	6.2	4.42e-13	3.35	0.2211	48.455	105600 ± 3600	12.76	0.085 ± 0.007
ANT18-02	s18023	6.5103	−75.7756	66.8	2.52e-13	3.81	0.2215	46.9147	61700 ± 2400	8.98	0.105 ± 0.009
ANT18-03	s18024	6.6788	−75.8101	120.2	1.44e-13	4.71	0.2060	47.7783	31500 ± 1600	11.55	0.261 ± 0.024
ANT18-04	s18025	7.0100	−76.2864	9.1	1.28e-13	4.58	0.2097	42.3884	32100 ± 1600	9.55	0.215 ± 0.019
ANT18-05	s18026	6.8814	−75.6659	132.3	1.73e-12	3.18	0.2098	45.1935	423900 ± 13500	16.29	0.026 ± 0.002
ANT18-06	s18027	7.0233	−75.6617	31.3	1.18e-13	4.44	0.2101	39.6815	31600 ± 1500	8.45	0.195 ± 0.017
ANT18-07	s18028	7.3504	−75.3361	118.2	3.13e-13	4.05	0.2105	44.2421	77500 ± 3200	5.74	0.055 ± 0.005
ANT18-08	s18029	7.2875	−75.3920	155.4	9.33e-14	4.51	0.2095	50.0194	19400 ± 1000	5.13	0.205 ± 0.017

[a] carrier ^{9}Be concentration $7.95*10^{-4}$ g/g
[b] normalized to the standards KN01-6-2 and KN01-5-3 with a nominal $^{10}Be/^{9}Be$ value of $5.35*10^{-12}$ and $6.32*10^{-12}$. Subtracted average blank ratio for corrections is $6.0*10^{-15} \pm 1.1*10^{-15}$.

into four geomorphic regions: southern CC, northern CC low relief, northern CC high relief, and the east-sloping surface of the northern CC.

CRN-derived erosion rates in the CC vary between geomorphic domains (Table 1). Above the flab slab subduction, samples on the low-relief-high-elevation surfaces have low average erosion rates

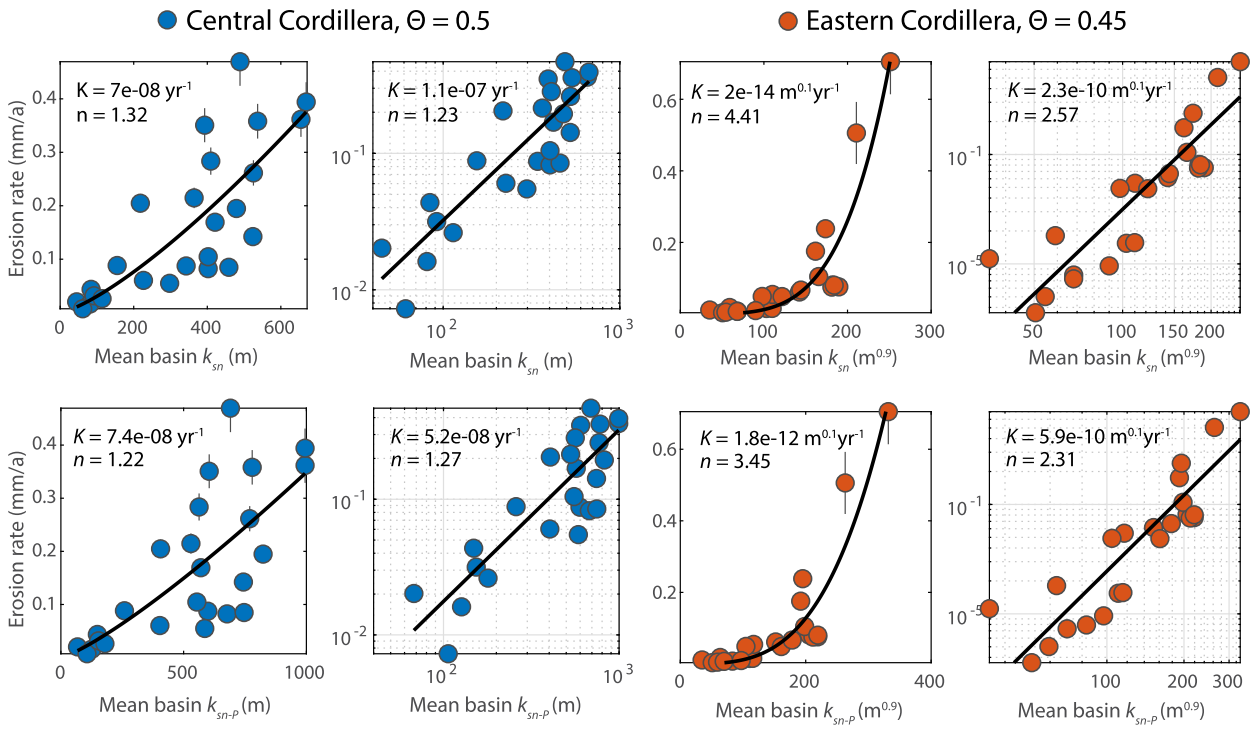

Fig. 3. Erosion rate versus k_{sn} and k_{sn-P} for the CC (left) and EC (right). Left panels show non-linear fit in linear space, right panels linear regression in log space. First row k_{sn}, second row k_{sn-P}. Note that due to different θ_{ref} the units for k_{sn} and K vary between the CC and EC.

of 0.017 ± 0.004 mm/a (Fig. 2). Average erosion rates on the east-sloping part of the low-relief surface are nearly three times higher (0.045 ± 0.007 mm/a), while average erosion rates in the high relief canyons of the northern CC are nearly an order of magnitude higher (0.138 ± 0.022 mm/a including one sample from the WC). The highest measured erosion rates are found south of the slab tear in the deeply incised valleys of the southern CC with an average of 0.316 ± 0.039 mm/a (Fig. 2). A Mann-Whitney test shows that the differences in erosion rates from geomorphic domains are statistically significant (Tab. S1).

4.2. Erosion rate - k_{sn} relationship

Both our newly determined erosion rates from the CC and the ones published by Struth et al. (2017) from the EC increase non-linearly with k_{sn} or k_{sn-P} (Fig. 3). In the CC, the regression parameters from non-linear regression models in linear space yield n-values of 1.22-1.32 and K of $7*10^{-8}$ - $1.1*10^{-7}$ (yr^{-1}). Values for n in the EC are higher (3.45 - 4.41) with a K of $2*10^{-14}$ - $1.8*10^{-12}$ ($m^{0.1}$ yr^{-1}). In contrast, the linear regression in log-space returns lower n and higher K values. Values of n and K depend on the regression method and the use of k_{sn} versus k_{sn-P}. K-values between the cordilleras cannot be compared directly due to the different units imparted by distinct regional θ_{ref}. We performed the same analysis using only steady-state catchments (see supplement) and found similar results (Fig. S3). In the CC, k_{sn} and k_{sn-P} regression parameters are similar, whereas in the EC, k_{sn-P} regressions yield lower n and higher K-values. This suggests that precipitation gradients can explain some non-linearity between channel steepness and erosion rate in the EC.

4.3. Inferred erosion rate maps

We used our new erosion rates from the CC and the ones published by Struth et al. (2017) for the EC to calculate inferred erosion rate maps for both cordilleras with our optimization approach. The distribution of measured CRN erosion rates is skewed, with many low and few high rates. Therefore, the weighted misfit function is biased towards fitting the lower end of CRN erosion rates where most data points exist. For the CC and EC data, this leads to an underestimation of high erosion rates (Fig. 4 A&D). In contrast, the non-weighted misfit function provides a better fit to the higher CRN erosion rates, but underestimates lower CRN erosion rates in the CC, and overestimates both intermediate and low CRN erosion rates in the EC (Fig. 4 B & E).

To minimize the influence of uneven CRN erosion rate data distribution on the regression, we attempted to bin the data into even-spaced erosion rate bins before performing our optimization. However, erosion rates in the EC were too unevenly distributed to cluster into erosion rate bins with more than three samples per bin. Therefore, we developed an alternative misfit function. For the tested parameter combinations of n and K, we converted the weighted and non-weighted misfit matrices to percentiles. We then added the two percentile matrices to determine the global minimum from both simulations. We refer to this method as 'semi-weighted'. Despite underprediction for high erosion rates, the semi-weighted fit performs best in the sense of fitting low and high erosion rates reasonably well in both Cordilleras (Fig. 4 C & F). The root mean square error (RMSE) of the semi-weighted is lower than the weighted approach (0.10 vs. 0.13, respectively), and significantly outperforms the non-weighted approach when considering the RMSE weighted by measurement uncertainty ($RMSE_w$, 5.89 vs. 10.98, respectively, Fig. 4). This demonstrates that the semi-weighted approach successfully strikes a balance between fitting the data according to their uncertainties while reducing the underestimation bias at high erosion rates. In the supplement, we show the n vs. K parameter space misfits for all fitting methods, which highlight the trade-offs between n and K (Fig. S4-S6). We take the parameters from our semi-weighted optimization as the best-fit model and use them to convert a k_{sn-P} map into an inferred erosion rate map (Fig. 5). To estimate uncertainties, we calculate maps of minimum and maximum erosion rate end members by taking

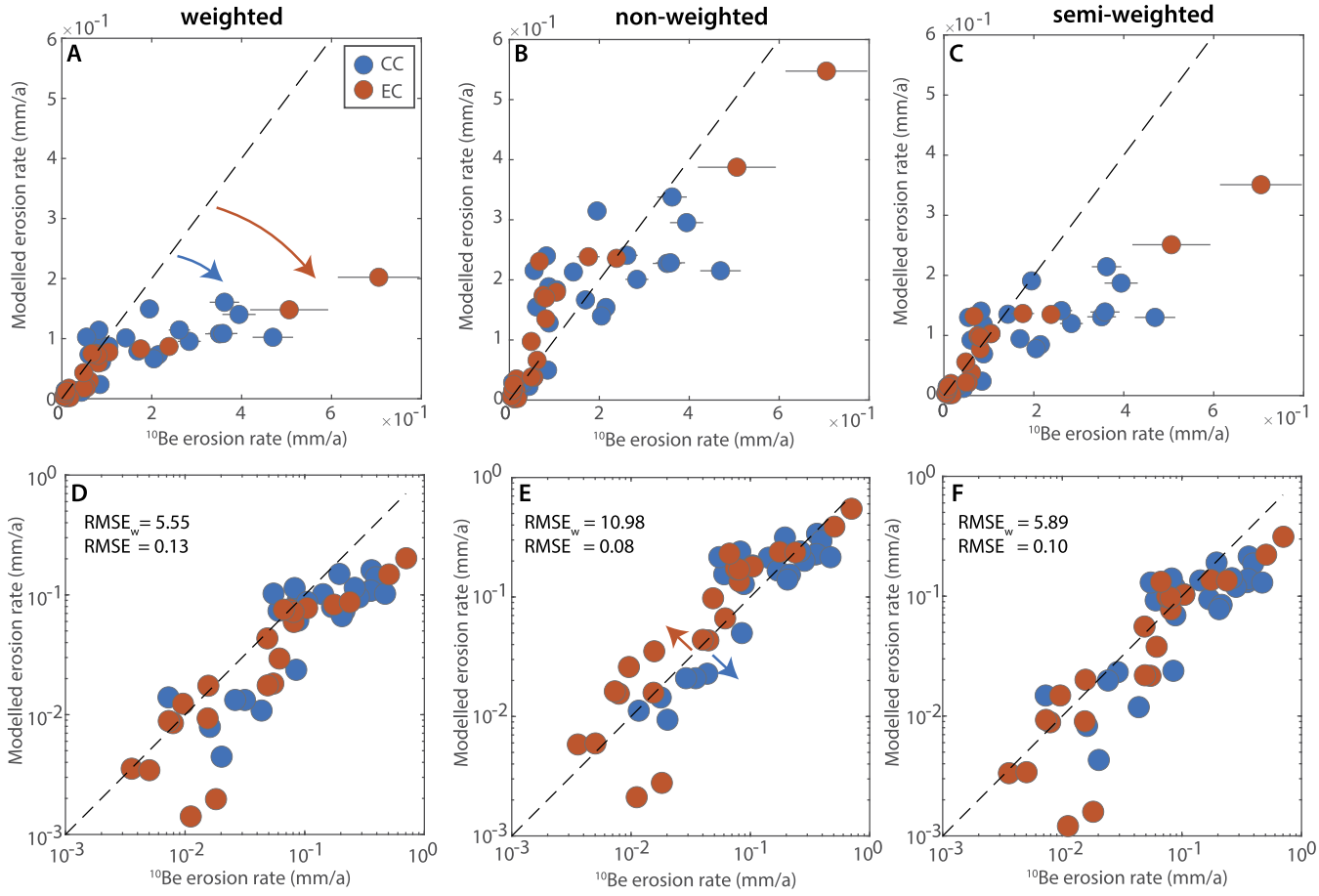

Fig. 4. Predicted versus measured erosion rates for the CC and EC for k_{sn-P} and different misfit functions. (*A*&*D*) Weighted misfit, (*B*&*E*) non-weighted misfit function, (*C*&*F*) semi-weighted misfit function. Data in the second row are plotted in log space to better visualize the fit of erosion rate data across scales. The root mean square error (RMSE) and RMSE with residuals weighted by the measurement uncertainty ($RMSE_w$) are shown in the lower plots. Colored arrows highlight biases in the optimization. Note that the semi-weighted approach partially mitigates the biases across the entire erosion rate range.

the minimum and maximum pixel values at each grid point across all methods (Fig. 5 B & C, difference to best-fit in Fig. S7).

In the CC, we find high and relatively uniform erosion rates in the south with a significant increase in erosion rate variability in the northern CC. Our inferred erosion rate maps indicate fast erosion of the downstream flanks of the Antioqueno Plateau in the northern CC compared to the slow erosion of the relic upland low-relief plateau surface (Fig. 5). In the southern CC, an area of lower inferred erosion rates is found near the crest (Fig. 5). However, this region has recently been linked to glacial planation based on the close correlation between the extent of this area and the altitude of moraines (Pérez-Consuegra et al., 2021b), highlighting that the interpretation of our maps should be limited to regions where fluvial erosion is the dominant erosion process on the time scale of landscape adjustment. In the EC, erosion rate variability is high and three important patterns can be observed: (1) the flanks of the EC erode rapidly and rim a slowly eroding central high plateau, (2) the eastern flank erodes more rapidly than the western flank, and (3) significant along-flank variation exists along the eastern EC, where erosion rates are high in the south and decrease towards the central part of the flank before increasing north towards the Cocuy range.

4.4. Sediment flux to foreland basins

We used the inferred erosion rate maps to estimate the total volume of eroded material for both Cordilleras by summing the pixel values of erosion rates (Table 2). This approach assumes that long-term sedimentary sinks in the CC and EC are negligible. Our preferred model (semi-weighted misfit) indicates 5.4 km^3/ka of erosion for the CC, with other models indicating a range from 4.1 to 8.7 km^3/ka. In the EC, a larger spread can be observed with precipitation-corrected values ranging from 9.8 to 28.4 and a preferred model estimate of 17.2 km^3/ka. Eroded volumes predicted by k_{sn} optimizations are similar (Tab. S2). Based on our best-fit models the total sediment export from the EC is nearly four times larger than from the CC.

We also predict sediment fluxes exported from the Northern Andes to neighboring sedimentary basins (Fig. 6). The total export from the EC into the Upper and Middle Magdalena Valley is nearly three times higher than from the CC (7.9 km^3/ka vs. 2.7 km^3/ka, respectively). The largest volume of sediments is exported to the Llanos foreland basin with 9.4 km^3/ka, whereas only about 0.6 km^3/ka are being supplied to the intermontane Cauca Valley.

5. Discussion

5.1. Limitations and time scale of erosion rate maps

Inferred erosion rate maps present a novel and versatile tool to study landscape evolution. Previous attempts used a coarse (5-km radius) moving window to map erosion values from the stream pixels to the hillslopes (Adams et al., 2020; Clementucci et al., 2022) or lacked the data to infer both n and K values (Clementucci et al., 2022). In contrast, our approach accounts not only for climatic gradients (Adams et al., 2020) but also for variations in

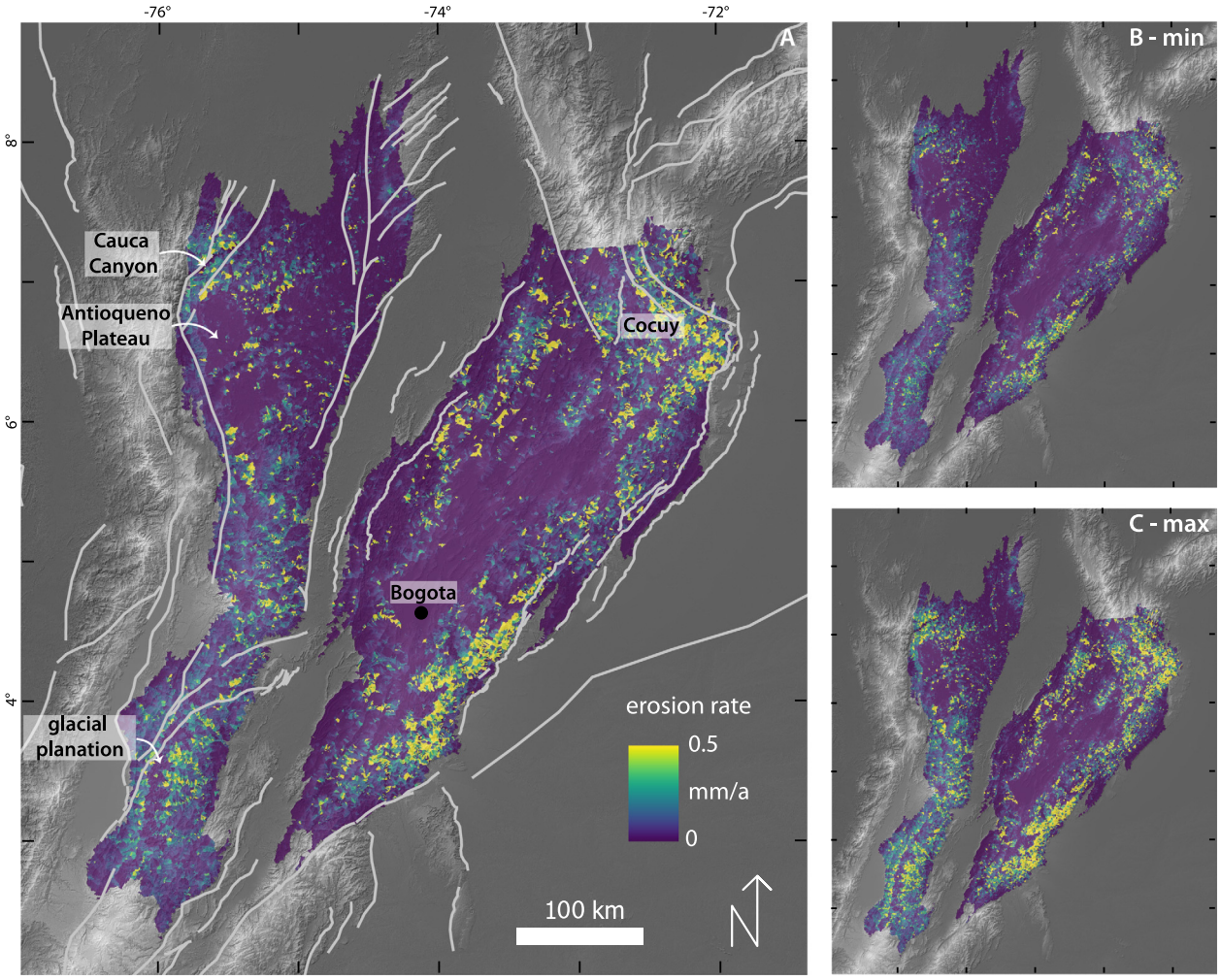

Fig. 5. (*A*) Inferred erosion rate map for CC and EC from the semi-weighted optimization with active faults superimposed. Minimum (*B*) and maximum (*C*) inferred erosion rates computed from the range in values of the three estimates. Color range for (*B*) and (*C*) is the same as in (*A*).

Table 2
Best fit optimization parameters and sediment flux based on k_{sn-P}.

Model	CC ($\theta = 0.5$)			EC ($\theta = 0.45$)		
	n	K	Sediment Flux (km^3/ka)	n	K	Sediment Flux (km^3/ka)
weighted	1.6	3.1E-09	4.1	2.8	1.2E-11	9.8
non-weighted	1.6	6.5E-09	8.7	3.2	2.7E-12	28.4
semi-weighted	1.8	1.0E-09	5.4	3.2	1.5E-12	17.2

major rock type between the two cordilleras. It also honors the natural division of the landscape into catchments and does not smooth erosion rate values across drainage divides. This is especially important when investigating landscapes with drainage reorganization, such as the Northern Andes (Struth et al., 2017; Pérez-Consuegra et al., 2021b), and allowed us to test the inferred erosion rate map for internal consistency by forward modeling catchment-average erosion rates.

Typically, only quasi-steady-state catchments and power-law regressions in $k_{sn} - E$ plots are used to derive n and K (e.g., Hilley et al., 2019; Adams et al., 2020), however, our optimization approach has several advantages: (1) it minimizes the influence of regression method selection (Fig. 3) (regression equation $E = K * {k_{sn}}^n$ vs. $\log(E) = \log(K) + n * \log(k_{sn})$), which can influence the parameter values (Xiao et al., 2011); (2) it does not require a mean basin k_{sn-P}-calculation, which could introduce biases in transient catchments, making it viable to include non-steady state catchments and thereby increasing the number of available data points for fitting, (3) it directly tests the consistency of the erosion rate map versus the measured data and (4) it ensures that calculations are weighted according to hillslope area by projecting k_{sn-P} onto the hillslopes and converting every pixel to an erosion rate. The improvement in (4) is important because, if hillslope erosion occurs at the same pace as adjacent channel incision, as is typically assumed, then calculations based on basin-averaged erosion rates must account for differences in hillslope area above local channel reaches, instead of using only channel-based k_{sn}-regressions to define n and K. Due to an uneven distribution of erosion rates, we found different best-fit parameters using weighted versus non-weighted optimization misfit functions. However, it may be possible to bin more uniformly distributed erosion rate data sets in other locations prior to optimization. In cases where the data distribution does not allow sufficient binning, we show that our semi-weighted approach yields a sat-

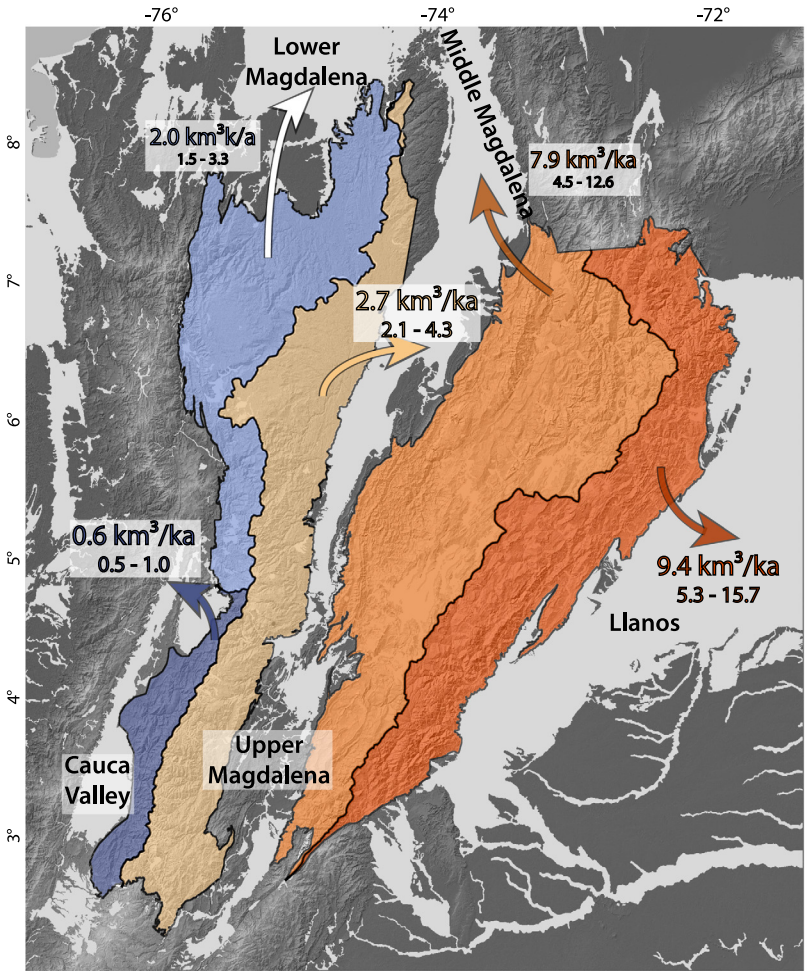

Fig. 6. Volumes of eroded material supplied from the CC and EC to neighboring sedimentary basins from different sides of the main drainage divide. Sedimentary basins are shaded gray. Different colors highlight the areas that drain to different sedimentary basins.

isfactory regression (Fig. 4). In any case, observed erosion rates should be compared to modeled ones to elucidate potential biases.

Our erosion rate maps combine millennial time scale ^{10}Be erosion rate measurements with modern precipitation data, which raises the question of whether these maps can be applied to interpret tectonic signals at million-year time scales. Paleo-precipitation models for the mid-Holocene and Last Glacial Maximum (Fick and Hijmans, 2017; Karger et al., 2023) indicate only moderate changes in precipitation, with relatively consistent spatial patterns throughout the study area (Fig. S10). Consequently, we assume that precipitation changes during glacial cycles have had a negligible impact on k_{sn-P} and by extension erosion rate. Moreover, in the southern CC, the steady-state river profiles (Pérez-Consuegra et al., 2021b) and our erosion rate maps, also suggest a lack of long-term changes in erosion to which the landscape is adjusting. Similarly, the spatial patterns in our erosion rate maps agree with patterns of total exhumation from balanced cross-sections (Fig. 7, discussed in section 5.2.2), sediment thicknesses in foreland basins (section 5.4), and exhumation rates from a thermochronologic compilation in the EC (Fig. S8) (Siravo et al., 2019). This evidence suggests that we can utilize our erosion rate maps for tectonic interpretations over a million-year time scale, despite the short-term nature of the measurements.

5.2. Tectonic implications of the erosion rate map

5.2.1. Central Cordillera

Low erosion rates on the plateau areas of the northern CC ringed by rapidly eroding downstream canyons, suggest that upstream plateau areas formed during a period of slower tectonic uplift and that a recent acceleration in uplift led to the incision of deep canyons. Based on the lack of internal deformation (Restrepo-Moreno et al., 2009), we assume simple block uplift and estimate the timing of relief generation and the acceleration in uplift rate. To achieve this, we divide the canyon relief by the difference between erosion rates on and below the plateau. For the northern CC, we determine the average erosion rate in the Cauca Canyon ($0.27^{+\ 0.13}_{-\ 0.08}$ mm/a) and on the plateau area above ($0.008^{+\ 0.010}_{-\ 0.001}$ mm/a). Together with the approximate 2200 m of canyon relief, we determine an acceleration of uplift around $8.3^{+\ 3.7}_{-\ 2.6}$ Ma ago (see supplement for more detail).

Our interpretations of landscape evolution in the CC agree with published thermochronologic data and thermal modeling. A Late Miocene erosion increase in the Cauca Canyon of the northern CC has been inferred from two 6-7 Ma Apatite (U-Th-Sm)/He ages (AHe) and inverse modeling (Pérez-Consuegra et al., 2022) and is in good agreement with our $8.3^{+\ 3.7}_{-\ 2.6}$ Ma uplift rate acceleration estimate. Previous thermochronological studies inferred surface uplift of the northern CC around 25 Ma (Restrepo-Moreno et al., 2009, 2019; Villagómez and Spikings, 2013), however, our erosion rate maps and the AHe ages from Pérez-Consuegra et al. (2022) suggest

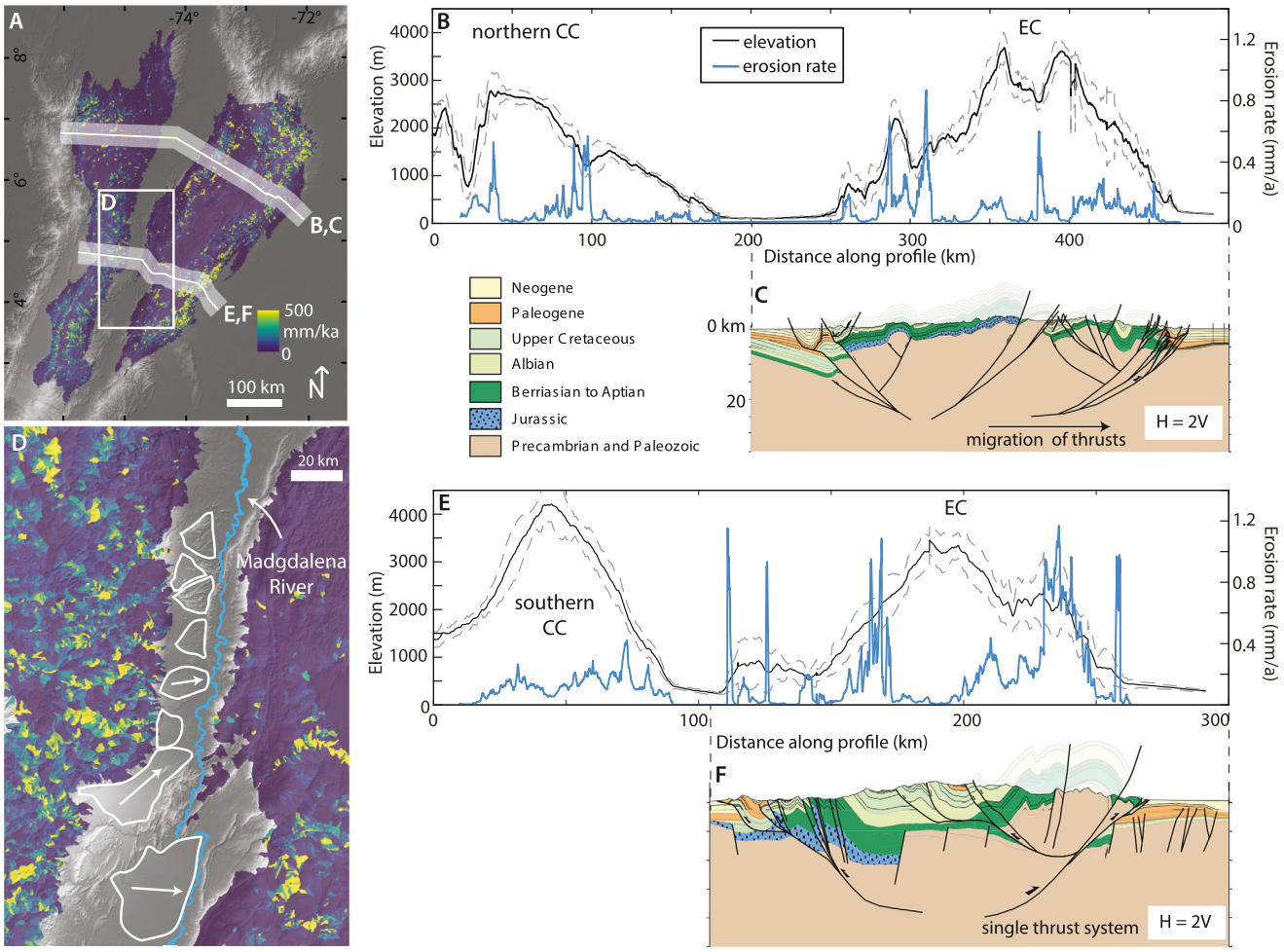

Fig. 7. Comparison between inferred erosion rate maps and balanced cross-sections. (*A*) Inferred erosion rate maps with the locations of swath profiles (*B*) and (*E*). (*B*) Swath profile across the northern CC and EC with elevation (black) and erosion rate (blue). (*C*) Balanced cross-section (Mora et al., 2013) showing several thrust systems causing exhumation on the eastern flank of the EC. (*D*) Higher erosion rates in southern CC compared to western EC, create alluvial fans (white outlines) that shift the course of the Magdalena to the eastern side of the Magdalena Valley. Map location highlighted in (*A*). (*E*) Swath profile across the southern CC and EC showing high inferred erosion rates on the eastern EC flank, independently supported by the balanced cross-section in (*F*).

that the Late Miocene uplift acceleration was missed in previous studies, due to insufficient late-stage exhumation at the sampling sites. This underscores the potential of erosion rate maps to detect recent tectonic changes in landscapes that may go unnoticed when relying solely on thermochronologic data.

Apart from the low erosion rate region near the crest, the southern CC is the area with the lowest erosion rate variability (Fig. 5), suggesting that this part of the mountain range is close to a topographic and erosional steady state. Results from thermochronologic data are more ambiguous with data from some locations suggesting steady exhumation and others a Late Miocene exhumation pulse (Villagómez and Spikings, 2013; Zapata et al., 2023). However, samples indicating a Miocene change in exhumation rate in the southern CC are located near the active Ibague fault. Therefore, we assume that these record the history of local faulting and do not necessarily reflect the exhumation of the southern CC as a whole. The increase of erosion and rock uplift in the northern CC in the Late Miocene coincides with the timing of slab flattening (Wagner et al., 2017), which, together with minor internal deformation (Restrepo-Moreno et al., 2009) suggests that the increase in uplift rate is due to a switch from negative to positive dynamic topography above the area of slab flattening, as modeled by Eakin et al. (2014) for the Peruvian flat slab. In contrast, the spatially uniform erosion rates of the southern CC suggest that no major changes in subduction geometry occurred over the time-scale of landscape adjustment.

5.2.2. Eastern Cordillera

Low erosion rates in the headwaters and fast erosion at low elevations suggests that rock uplift rates in the EC were slow in the past and accelerated more recently, leading to transient landscape adjustment similar to that observed in the northern CC (Struth et al., 2015, 2017). In the southeastern EC, uplift has been focused on a single thrust system (Fig. 7C). Hence, we also estimate relief generation and uplift acceleration by assuming a simple block uplift with canyon incision as in the northern CC. We determine a plateau erosion rate of $0.006^{+\ 0.005}_{-\ 0.001}$ mm/a and a canyon erosion rate of $0.43^{+\ 0.28}_{-\ 0.16}$ mm/a, resulting in a relief generation and uplift acceleration estimate of $6.9^{+\ 2.8}_{-\ 4.1}$ Ma (see supplement). Several thermochronologic and geologic studies also suggest an increase in exhumation rates and mountain building since the Late Miocene (Mora et al., 2008, 2013; Siravo et al., 2019), which agrees with findings from pollen studies near Bogota indicating a rise from lowland elevations to > 2 km within the same time period (Hooghiemstra et al., 2006). We note, though, that this pollen-based estimate of paleo-elevation is debated (Molnar and Perez-Angel, 2021). Furthermore, a faster eroding and hence faster uplifting eastern flank is consistent with the higher density of shallow

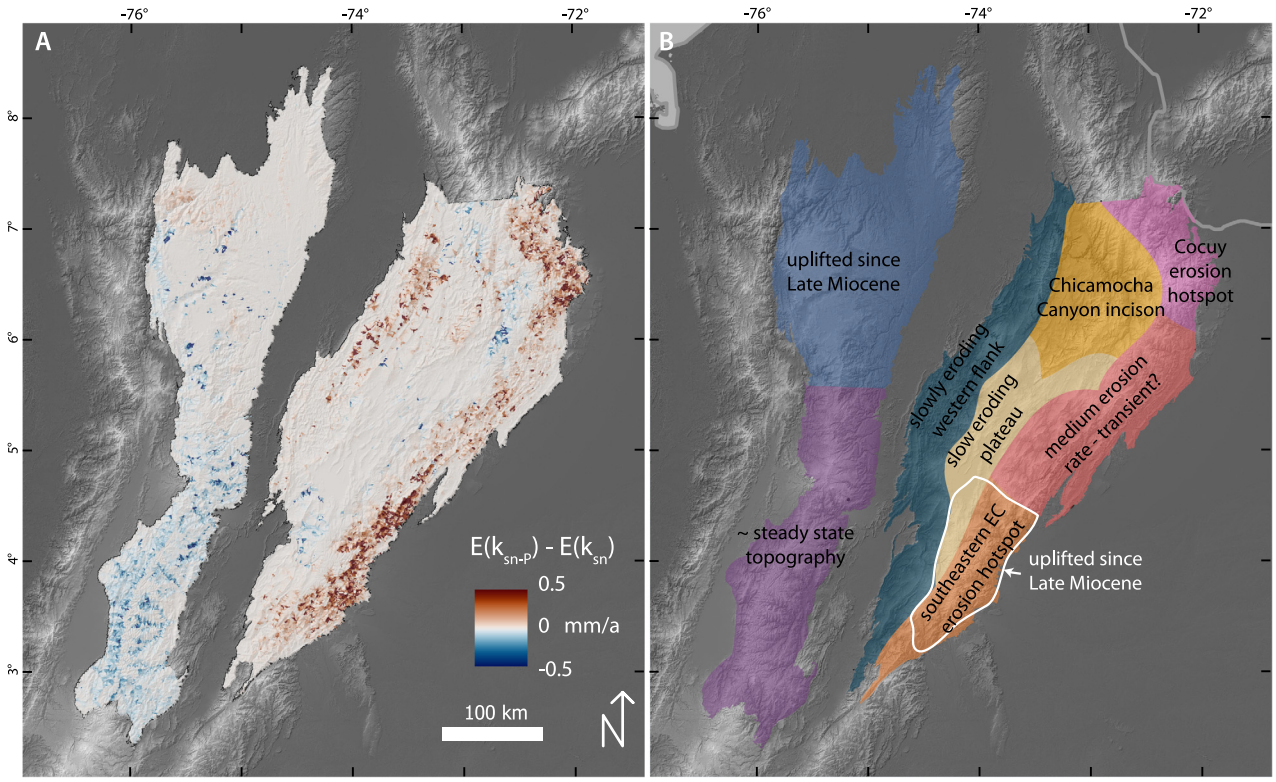

Fig. 8. (*A*) Difference in erosion rate between erosion rate maps based on k_{sn-P} and k_{sn}. Positive values indicate higher erosion rates predicted by k_{sn-P}, and vice versa. (*B*) Different geomorphic regions and their characteristics identified based on our erosion rate map. Note positive values along the southeastern and northeastern EC flank in (*A*) highlight that only k_{sn-P} predicts independently documented erosional hotspots.

earthquakes recorded along the eastern flank (Fig. 1A). Moreover, a balanced cross-section (Mora et al., 2013) shows substantially deeper exhumation of rocks on the eastern flank, where inferred erosion rates are highest (Fig. 7F). This suggests elevated erosion rates on the southeastern EC flank have persisted long enough to create asymmetrical unroofing of ∼4 kilometers compared to the western flank (Fig. 7F).

In the EC, two regions stand out as erosional hotspots: the Cocuy Range in the northern EC and the southeastern flank of the EC. Both loci of erosion coincide with locations of rapid exhumation, with AFT ages $<$ 10 Ma and AHe ages $<$ 5 Ma (Mora et al., 2008, 2015; Siravo et al., 2018; Pérez-Consuegra et al., 2021a) (Fig. S8). The central portion of the eastern EC flank has lower inferred erosion rates and coincides with an area where the orogen widens and several parallel thrust systems are active simultaneously (Jimenez et al., 2013) (Fig. 7C). This suggests that slower erosion rates in this region may be related to more distributed exhumation, occurring primarily along new thrust faults propagating towards the foreland. In this region, balanced cross-sections also indicate more distributed unroofing (Fig. 7C). The simultaneous activity of several thrust sheets leads to a transient slope reduction of the flank until the main deformation front has migrated basinward. The consistent spatial patterns between our erosion rate maps and tectonic data (Fig. S8) suggest that erosion rate maps can be used to identify transient adjustments of thrust tectonics during orogen growth.

5.2.3. Magdalena Valley

In the southern part of the Middle Magdalena Valley, inferred erosion rates in the CC are higher than in the corresponding western flank of the EC (Fig. 7). This might explain that the current geographic distribution of Plio-Quaternary alluvial fans from the CC seems to push the Magdalena River to the eastern side of its intermontane valley. This is likely a consequence of the higher sediment flux from the CC producing larger alluvial fans that deflect the river eastwards (Fig. 7D).

5.3. Variations in climate and erosion parameters

Our optimization results show a large difference in exponent n, with $n > 3$ in the EC, and < 2 in the CC (Table 2). This means that in the CC, small differences in k_{sn-P} yield only modest differences in erosion rate, whereas small differences in k_{sn-P} in the EC correspond to substantial differences in erosion rate due to the larger exponent. The difference in n could be related to differences in dominant incision mechanism or the presence of incision thresholds in combination with variations in discharge variability and/or channel sediment characteristics (Whipple et al., 2000; Lague et al., 2005).

A comparison of erosion rate maps based on k_{sn-P} and k_{sn} suggests that only maps based on k_{sn-P} predict erosional hotspots in the southeastern EC and the Cocuy (Fig. 8, S8). In the southern CC, higher erosion rates based on k_{sn} compared to k_{sn-P} (Fig. 8) indicate that low precipitation rates in this area may lead to an overestimation of rock uplift if only topography is considered. This highlights the importance of including rainfall into k_{sn} calculations (Adams et al., 2020) and underscores the significant influence of climate on relationships between erosion and topography in the Northern Andes.

By accounting for spatial variations in erosion parameters and climate gradients simultaneously, our analyses reveal important local variations in tectonic forcing that would otherwise be obscured in traditional river profile analyses. For instance, variations in k_{sn} along the eastern flank of the EC are minor (Fig. S9A), however, our erosion rate maps and independent thermochronology and neotectonic data suggest substantial variations in uplift rate along strike (Mora et al., 2010). This implies that the combined effects of large exponent n and precipitation patterns in the EC lead to a situa-

tion where subtle differences in k_{sn} along the eastern EC translate into substantial gradients in inferred erosion rates and rock uplift, highlighting the importance of moving beyond k_{sn} or k_{sn-P} analyses.

5.4. Sedimentation in foreland basins and coeval tectonic processes

The predicted sedimentary fluxes from our inferred erosion rate maps (Fig. 6) agree well with the relative stratigraphic thicknesses deposited since the Neogene in the adjacent foreland basins. The highest thicknesses and volumes of preserved Neogene to recent sedimentary units (ca. 4 km, Reyes-Harker et al., 2015) have been documented in the Llanos foreland basin adjacent to the eastern flank of the EC (Hermeston and Nemčok, 2013; Reyes-Harker et al., 2015). The second-highest volumes of preserved Neogene to recent sedimentary units have been documented in the Middle Magdalena intramountain Basin with a thickness of up to 2 km (Moreno et al., 2013; Reyes-Harker et al., 2015). We have shown that sediment export in the southern Middle Magdalena Valley is greater from the CC than from the western EC flank (Fig. 7D). However, the total flux to the Middle Magdalena Valley from the EC is greater due to the large amount of sediment being delivered to the northern Middle Magdalena Valley by the Sogamoso River, which drains a significant portion of the EC plateau area. In contrast, the preservation of Neogene to recent sedimentary units is minor in the Cauca Valley west of the Central Cordillera (Suter et al., 2008), consistent with our predictions.

In the CC, sediment fluxes are almost identical between the eastern and western flanks, suggesting symmetrical uplift of the orogen. In contrast, in the EC, asymmetrical erosion and sediment export suggest higher rates of tectonic uplift along the eastern flank of the EC. This interpretation is consistent with the off-center location of the main drainage divide separating the Upper Magdalena Valley and Llanos Basin (Fig. 6). In mountain ranges experiencing asymmetric uplift, the main drainage divide should move towards the mountain side with higher uplift rates (He et al., 2021). Higher uplift rates along the eastern flank of the EC may have congruently shifted the main drainage divide to the east.

Several structural studies have concluded that deformation along the western flank of the EC commenced in the Eocene/Oligocene (Gómez et al., 2003; Horton et al., 2010), which suggests that the locus of deformation and uplift has moved eastward since the Late Miocene (Mora et al., 2013; Siravo et al., 2018). It remains unclear, however, what drove eastward migration of deformation and Late Miocene to recent surface uplift. It has been hypothesized that the location of widening north of 4.5°N may be related to inherited structures. It has also been postulated that faster exhumation rates in the eastern EC flank are linked to a deeper rifting in this region (Mora et al., 2015; Pérez-Consuegra et al., 2021a). However, this does not explain the temporal shift in uplift from west to east revealed by our erosion maps and other geochronologic data. Based on the low crustal thickness of the northern EC and the symmetric widening of the EC north of ∼4.5°N, together with the Late Miocene timing we found for accelerated surface uplift, we speculate that Late Miocene slab flattening not only caused dynamic uplift (Siravo et al., 2019) but also shifted deformation eastward to the eastern flank of the EC, consistent with the predictions of geodynamic models (Martinod et al., 2020). This would suggest that changes in subduction geometry over the Cenozoic were the main driver of topographic evolution of the Northern Andes with a potential overprint by inherited tectonic structures.

6. Summary and conclusions

We determined CRN erosion rates and used them together with published data and interpolation methods to generate inferred erosion rate maps of the Northern Andes. Our main findings are:

(1) Subduction geometry exerts first-order control on spatial and temporal patterns of erosion in the Northern Andes. CRN-derived erosion rates are highest in the southern CC above the normal slab subduction; erosion rates on the plateau surfaces in the northern CC are slow, with faster rates below major knickpoints. From the distribution of erosion rates, we estimate a Late Miocene increase in rock uplift in the northern CC likely related to dynamic uplift following slab flattening.
(2) Topographic signatures of landscape steady state and transience provide surface evidence of changes in subduction geometry along the northern Andean margin. The southern CC above the normal slab segment exhibits a steady-state topography which suggests that there were no major changes in subduction geometry during the Neogene, whereas the EC shows a pronounced topographic and erosional disequilibrium.
(3) Differences between erosion rates in the headwaters and at the mountain front suggest temporal changes in tectonic forcing. Fast erosion of the EC flanks and low erosion of the interior Altiplano suggest strong topographic growth; based on our calculations major surface uplift of the southeastern flank commenced in the Late Miocene.
(4) Faster erosion rates in the eastern EC compared to the western flank show asymmetric tectonic uplift, in agreement with thermochronometric and geological data.
(5) Along strike variations in erosion rate on the eastern flank of the EC are most likely linked to different stages of wedge growth and fault stepping.
(6) Spatial differences in climate and erosional parameters highlight the importance of moving from k_{sn} analysis to inferred erosion rate maps to extract tectonic and erosional information from topography.
(7) Sediment flux from the EC is nearly four times higher than from the CC. The Llanos foreland basin receives the highest sediment flux of all foreland basins in Colombia, providing a large amount of nutrients to the northern Andean foreland biodiversity hotspot.

CRediT authorship contribution statement

Richard F. Ott: Conceptualization, Funding acquisition, Investigation, Methodology, Writing – original draft. **Nicolás Pérez-Consuegra:** Investigation, Writing – review & editing. **Dirk Scherler:** Investigation, Writing – review & editing. **Andrés Mora:** Resources, Writing – review & editing. **Kimberly L. Huppert:** Investigation, Writing – review & editing. **Jean Braun:** Writing – review & editing. **Gregory D. Hoke:** Investigation, Writing – review & editing. **Jose R. Sandoval Ruiz:** Investigation.

Declaration of competing interest

The authors declare that they have no known competing financial interests or personal relationships that could have appeared to influence the work reported in this paper.

Data availability

All data to reproduce the findings of this study are available within the main text, supplement, and cited literature. An example script to replicate the calculation of our best-fit erosion rate map can be found at doi.org/10.5281/ZENODO.8021046.

Acknowledgements

R.F.O. was supported by the Swiss National Science Foundation fellowship, grant number P2EZP2_191866. NPC was supported by grant No. 4.448 from the Fundación para la promoción de la investigación y la tecnología – Banco de la República (Colombia). We thank two anonymous reviewers for providing comments that helped to improve this manuscript.

Appendix A. Supplementary material

Supplementary material related to this article can be found online at https://doi.org/10.1016/j.epsl.2023.118354.

References

Adams, B.A., Whipple, K.X., Forte, A.M., Heimsath, A.M., Hodges, K.V., 2020. Climate controls on erosion in tectonically active landscapes. Sci. Adv. 6, eaaz3166. https://doi.org/10.1126/sciadv.aaz3166.

Anderson, V.J., Horton, B.K., Saylor, J.E., Mora, A., Tesón, E., Breecker, D.O., Ketcham, R.A., 2016. Andean topographic growth and basement uplift in southern Colombia: implications for the evolution of the Magdalena, Orinoco, and Amazon river systems. Geosphere 12, 1235–1256. https://doi.org/10.1130/GES01294.1.

Anderson, V.J., Saylor, J.E., Shanahan, T.M., Horton, B.K., 2015. Paleoelevation records from lipid biomarkers: application to the tropical Andes. Bull. Geol. Soc. Am. 127, 1604–1616. https://doi.org/10.1130/B31105.1.

Beaumont, C., Fullsack, P., Hamilton, J., 1992. Erosional control of active compressional orogens. Thrust Tecton., 1–18. https://doi.org/10.1007/978-94-011-3066-0_1.

Clementucci, R., Ballato, P., Siame, L.L., Faccenna, C., Yaaqoub, A., Essaifi, A., Leanni, L., Guillou, V., 2022. Lithological control on topographic relief evolution in a slow tectonic setting (Anti-Atlas, Morocco). Earth Planet. Sci. Lett. 596, 117788. https://doi.org/10.1016/J.EPSL.2022.117788.

Clubb, F.J., Mudd, S.M., Hurst, M.D., Grieve, S.W.D., 2020. Differences in Channel and Hillslope Geometry Record a Migrating Uplift Wave at the Mendocino Triple Junction, vol. 48. Geology, California, USA, pp. 184–188.

Cooper, M.A., et al., 1995. Basin Development and Tectonic History of the Llanos Basin, Eastern Cordillera, and Middle Magdalena Valley, vol. 79. AAPG Bulletin, Colombia, pp. 1421–1442.

DiBiase, R.A., Whipple, K.X., Heimsath, A.M., Ouimet, W.B., 2010. Landscape form and millennial erosion rates in the San Gabriel Mountains, CA. Earth Planet. Sci. Lett. 289, 134–144. https://doi.org/10.1016/j.epsl.2009.10.036.

Eakin, C.M., Lithgow-Bertelloni, C., Dávila, F.M., 2014. Influence of Peruvian flat-subduction dynamics on the evolution of western Amazonia. Earth Planet. Sci. Lett. 404, 250–260. https://doi.org/10.1016/j.epsl.2014.07.027.

Fick, S.E., Hijmans, R.J., 2017. WorldClim 2: new 1-km spatial resolution climate surfaces for global land areas. Int. J. Climatol. 37, 4302–4315. https://doi.org/10.1002/joc.5086.

Flint, J.J., 1974. Stream gradient as a function of order, magnitude, and discharge. Water Resour. Res. 10, 969–973. https://doi.org/10.1029/WR010i005p00969.

Gómez, E., Jordan, T.E., Allmendinger, R.W., Cardozo, N., 2005. Development of the Colombian foreland-basin system as a consequence of diachronous exhumation of the northern Andes. Bull. Geol. Soc. Am. 117, 1272–1292. https://doi.org/10.1130/B25456.1.

Gómez, E., Jordan, T.E., Allmendinger, R.W., Hegarty, K., Kelley, S., Heizler, M., 2003. Controls on architecture of the Late Cretaceous to Cenozoic southern Middle Magdalena Valley Basin, Colombia. Bull. Geol. Soc. Am. 115, 131–147. https://doi.org/10.1130/0016-7606(2003)115<0131:COAOTL>2.0.CO;2.

Gomez, J., Montes, N.E., 2020. Geological Map of Colombia 2020. Scale 1:1 000 000. Servicio Geológico Colombiano. 2 sheets. Bogota.

Granger, D.E., Kirchner, J.W., Finkel, R., 1996. Spatially averaged long-term erosion rates measured from in situ-produced cosmogenic nuclides in alluvial sediment. J. Geol. 104, 249–257. https://doi.org/10.1086/629823.

He, C., Yang, C.J., Turowski, J.M., Rao, G., Roda-Boluda, D.C., Yuan, X.P., 2021. Constraining tectonic uplift and advection from the main drainage divide of a mountain belt. Nat. Commun. 12 (1). https://doi.org/10.1038/s41467-020-20748-2, 1–10.

Hermeston, S., Nemčok, M., 2013. Thick-skin orogen-foreland interactions and their controlling factors, Northern Andes of Colombia. Geol. Soc. (Lond.) Spec. Publ. 377, 443–471. https://doi.org/10.1144/SP377.16.

Hilley, G.E., Porder, S., Aron, F., Baden, C.W., Johnstone, S.A., Liu, F., Sare, R., Steelquist, A., Young, H.H., 2019. Earth's topographic relief potentially limited by an upper bound on channel steepness. Nat. Geosci. 12, 828–832. https://doi.org/10.1038/s41561-019-0442-3.

Hooghiemstra, H., Wijninga, V.M., Cleef, A.M., 2006. The paleobotanical record of Colombia: implications for biogeography and biodiversity 1. Ann. Mo. Bot. Gard. 93, 297–325. https://doi.org/10.3417/0026-6493(2006)93[297:tproci]2.0.co;2.

Hoorn, C., et al., 2010. Amazonia through time: Andean uplift, climate change, landscape evolution, and biodiversity. Science 330, 927–931. https://doi.org/10.1126/science.1194585.

Horton, B.K., Parra, M., Saylor, J.E., Nie, J., Mora, A., Torres, V., Stockli, D.F., Strecker, M.R., 2010. Resolving uplift of the northern Andes using detrital zircon age signatures. GSA Today 20, 4–9. https://doi.org/10.1130/GSATG76A.1.

Howard, A.D., 1994. A detachment-limited model of drainage basin evolution. Water Resour. Res. 30, 2261–2285. https://doi.org/10.1029/94WR00757.

Hurst, M.D., Grieve, S.W.D., Clubb, F.J., Mudd, S.M., 2019. Detection of channel-hillslope coupling along a tectonic gradient. Earth Planet. Sci. Lett. 522, 30–39. https://doi.org/10.1016/j.epsl.2019.06.018.

Jimenez, L., Mora, A., Casallas, W., Silva, A., Tesón, E., Tamara, J., Namson, J., Higuera-Díaz, I.C., Lasso, A., Stockli, D., 2013. Segmentation and growth of foothill thrust-belts adjacent to inverted grabens: the case of the Colombian Llanos foothills. Geol. Soc. (Lond.) Spec. Publ. 377, 189–220. https://doi.org/10.1144/SP377.11.

Karger, D.N., Conrad, O., Böhner, J., Kawohl, T., Kreft, H., Soria-Auza, R.W., Zimmermann, N.E., Linder, H.P., Kessler, M., 2017. Climatologies at high resolution for the Earth's land surface areas. Sci. Data 4. https://doi.org/10.1038/SDATA.2017.122.

Karger, D.N., Nobis, M.P., Normand, S., Graham, C.H., Zimmermann, N.E., 2023. CHELSA-TraCE21k - high-resolution (1 km) downscaled transient temperature and precipitation data since the Last Glacial Maximum. Clim. Past 19, 439–456. https://doi.org/10.5194/CP-19-439-2023.

Kirby, E., Whipple, K.X., 2012. Expression of active tectonics in erosional landscapes. J. Struct. Geol. 44, 54–75. https://doi.org/10.1016/J.JSG.2012.07.009.

Lague, D., Hovius, N., Davy, P., 2005. Discharge, discharge variability, and the bedrock channel profile. J. Geophys. Res., Earth Surf. 110, 4006. https://doi.org/10.1029/2004JF000259.

Martinod, J., Gérault, M., Husson, L., Regard, V., 2020. Widening of the Andes: an interplay between subduction dynamics and crustal wedge tectonics. Earth-Sci. Rev. 204, 103170. https://doi.org/10.1016/j.earscirev.2020.103170.

Molnar, P., Perez-Angel, L.C., 2021. Constraints on the paleoelevation history of the Eastern Cordillera of Colombia from its palynological record. Geosphere 17, 1333–1352. https://doi.org/10.1130/GES02328.1.

Mora-Páez, H., Mencin, D.J., Molnar, P., Diederix, H., Cardona-Piedrahita, L., Peláez-Gaviria, J.R., Corchuelo-Cuervo, Y., 2016. GPS velocities and the construction of the Eastern Cordillera of the Colombian Andes. Geophys. Res. Lett. 43, 8407–8416. https://doi.org/10.1002/2016GL069795.

Mora, A., et al., 2013. Inversion tectonics under increasing rates of shortening and sedimentation: Cenozoic example from the Eastern Cordillera of Colombia. Geol. Soc. (Lond.) Spec. Publ. 377, 411–442. https://doi.org/10.1144/SP377.6.

Mora, A., Casallas, W., Ketcham, R.A., Gomez, D., Parra, M., Namson, J., Stockli, D., Almendral, A., Robles, W., Ghorbal, B., 2015. Kinematic restoration of contractional basement structures using thermokinematic models: a key tool for petroleum system modeling. AAPG Bull. 99, 1575–1598. https://doi.org/10.1306/04281411108.

Mora, A., Parra, M., Strecker, M.R., Kammer, A., Dimaté, C., Rodríguez, F., 2006. Cenozoic contractional reactivation of Mesozoic extensional structures in the Eastern Cordillera of Colombia. Tectonics 25. https://doi.org/10.1029/2005TC001854.

Mora, A., Parra, M., Strecker, M.R., Sobel, E.R., Hooghiemstra, H., Torres, V., Jaramillo, J.V., 2008. Climatic forcing of asymmetric orogenic evolution in the Eastern Cordillera of Colombia. GSA Bull. 120, 930–949. https://doi.org/10.1130/B26186.1.

Mora, A., Parra, M., Strecker, M.R., Sobel, E.R., Zeilinger, G., Jaramillo, C., Da Silva, S.F., Blanco, M., 2010. The eastern foothills of the Eastern Cordillera of Colombia: an example of multiple factors controlling structural styles and active tectonics. GSA Bull. 122, 1846–1864. https://doi.org/10.1130/B30033.1.

Moreno, N., et al., 2013. Interaction between thin- and thick-skinned tectonics in the foothill areas of an inverted graben. The Middle Magdalena Foothill belt. Geol. Soc. (Lond.) Spec. Publ. 377, 221–255. https://doi.org/10.1144/SP377.18.

Ott, R.F., 2023. Erosion rate map example script. https://doi.org/10.5281/ZENODO.8021046.

Ouimet, W.B., Whipple, K.X., Granger, D.E., 2009. Beyond threshold hillslopes: channel adjustment to base-level fall in tectonically active mountain ranges. Geology 37, 579–582. https://doi.org/10.1130/G30013A.1.

Pérez-Consuegra, N., Hoke, G.D., Fitzgerald, P., Mora, A., Sobel, E.R., Glodny, J., 2022. Late Miocene-Pliocene onset of fluvial incision of the Cauca River Canyon in the Northern Andes. GSA Bull. https://doi.org/10.1130/B36047.1.

Pérez-Consuegra, N., Hoke, G.D., Mora, A., Fitzgerald, P., Sobel, E.R., Sandoval, J.R., Glodny, J., Valencia, V., Parra, M., Zapata, S., 2021a. The case for tectonic control on erosional exhumation on the tropical northern Andes based on thermochronology data. Tectonics 40, e2020TC006652. https://doi.org/10.1029/2020TC006652.

Pérez-Consuegra, N., Ott, R.F., Hoke, G.D., Galve, J.P., Pérez-Peña, V., Mora, A., 2021b. Neogene variations in slab geometry drive topographic change and drainage reorganization in the Northern Andes of Colombia. Glob. Planet. Change 206, 103641. https://doi.org/10.1016/j.gloplacha.2021.103641.

Restrepo-Moreno, S.A., Foster, D.A., Bernet, M., Min, K., Noriega, S., 2019. Morphotectonic and orogenic development of the northern Andes of Colombia. https://doi.org/10.1007/978-3-319-76132-9_11. pp. 749–832.

Restrepo-Moreno, S.A., Foster, D.A., Stockli, D.F., Parra-Sánchez, L.N., 2009. Long-term erosion and exhumation of the "Altiplano Antioqueño", Northern Andes (Colombia) from apatite (U-Th)/He thermochronology. Earth Planet. Sci. Lett. 278, 1–12. https://doi.org/10.1016/j.epsl.2008.09.037.

Reyes-Harker, A., et al., 2015. Cenozoic paleogeography of the Andean foreland and retroarc hinterland of Colombia. AAPG Bull. 99, 1407–1453. https://doi.org/10.1306/06181411110.

Rodriguez-Muñoz, E., Montes, C., Rojas-Runjaic, F.J.M., Crawford, A.J., 2022. Synthesis of geological data and comparative phylogeography of lowland tetrapods suggests recent dispersal through lowland portals crossing the Eastern Andean Cordillera. PeerJ 10, e13186. https://doi.org/10.7717/PEERJ.13186/SUPP-6.

Schildgen, T.F., Cosentino, D., Bookhagen, B., Niedermann, S., Yildirim, C., Echtler, H., Wittmann, H., Strecker, M.R., 2012. Multi-phased uplift of the southern margin of the Central Anatolian plateau, Turkey: a record of tectonic and upper mantle processes. Earth Planet. Sci. Lett. 317-318, 85–95. https://doi.org/10.1016/J.EPSL.2011.12.003.

Schwanghart, W., Scherler, D., 2017. Bumps in river profiles: uncertainty assessment and smoothing using quantile regression techniques. Earth Surf. Dyn. 5, 821–839. https://doi.org/10.5194/esurf-5-821-2017.

Schwanghart, W., Scherler, D., 2014. Short Communication: TopoToolbox 2 – MATLAB-based software for topographic analysis and modeling in Earth surface sciences. Earth Surf. Dyn. 2, 1–7. https://doi.org/10.5194/esurf-2-1-2014.

Siravo, G., Faccenna, C., Gérault, M., Becker, T.W., Fellin, M.G., Herman, F., Molin, P., 2019. Slab flattening and the rise of the Eastern Cordillera, Colombia. Earth Planet. Sci. Lett. 512, 100–110. https://doi.org/10.1016/j.epsl.2019.02.002.

Siravo, G., Fellin, M.G., Faccenna, C., Bayona, G., Lucci, F., Molin, P., Maden, C., 2018. Constraints on the Cenozoic Deformation of the Northern Eastern Cordillera, Colombia. Tectonics 37, 4311–4337. https://doi.org/10.1029/2018TC005162.

Struth, L., Babault, J., Teixell, A., 2015. Drainage reorganization during mountain building in the river system of the Eastern Cordillera of the Colombian Andes. Geomorphology 250, 370–383. https://doi.org/10.1016/j.geomorph.2015.09.012.

Struth, L., Teixell, A., Owen, L.A., Babault, J., 2017. Plateau reduction by drainage divide migration in the Eastern Cordillera of Colombia defined by morphometry and 10Be terrestrial cosmogenic nuclides. Earth Surf. Process. Landf. 42, 1155–1170. https://doi.org/10.1002/esp.4079.

Sun, M., Bezada, M.J., Cornthwaite, J., Prieto, G.A., Niu, F., Levander, A., 2022. Overlapping slabs: untangling subduction in NW South America through finite-frequency teleseismic tomography. Earth Planet. Sci. Lett. 577, 117253. https://doi.org/10.1016/j.epsl.2021.117253.

Suter, F., Sartori, M., Neuwerth, R., Gorin, G., 2008. Structural imprints at the front of the Chocó-Panamá indenter: field data from the North Cauca Valley Basin, Central Colombia. Tectonophysics 460, 134–157. https://doi.org/10.1016/j.tecto.2008.07.015.

Taboada, A., Rivera, L.A., Fuenzalida, A., Cisternas, A., Philip, H., Bijwaard, H., Olaya, J., Rivera, C., 2000. Geodynamics of the northern Andes. Tectonics 19, 787–813.

Trenkamp, R., Kellogg, J.N., Freymueller, J.T., Mora, H.P., 2002. Wide plate margin deformation, southern Central America and northwestern South America, CASA GPS observations. J. South Am. Earth Sci. 15, 157–171. https://doi.org/10.1016/S0895-9811(02)00018-4.

U.S. Geological Survey, 2020. Earthquake catalog. https://earthquake.usgs.gov/earthquakes/search/. (Accessed June 2020).

Veloza, G., Styron, R., Taylor, M., 2012. Open-source archive of active faults for northwest South America. GSA Today 22, 4–10. https://doi.org/10.1130/GSAT-G156A.1.

Villagómez, D., Spikings, R., 2013. Thermochronology and tectonics of the Central and Western Cordilleras of Colombia: early Cretaceous-Tertiary evolution of the Northern Andes. Lithos 160-161, 228–249. https://doi.org/10.1016/j.lithos.2012.12.008.

Villagómez, D., Spikings, R., Magna, T., Kammer, A., Winkler, W., Beltrán, A., 2011. Geochronology, geochemistry and tectonic evolution of the Western and Central cordilleras of Colombia. Lithos 125, 875–896. https://doi.org/10.1016/J.LITHOS.2011.05.003.

Wagner, L.S., Jaramillo, J.S., Ramírez-Hoyos, L.F., Monsalve, G., Cardona, A., Becker, T.W., 2017. Transient slab flattening beneath Colombia. Geophys. Res. Lett. 44, 6616–6623. https://doi.org/10.1002/2017GL073981.

Whipple, K.X., Forte, A.M., DiBiase, R.A., Gasparini, N.M., Ouimet, W.B., 2017. Timescales of landscape response to divide migration and drainage capture: implications for the role of divide mobility in landscape evolution. J. Geophys. Res., Earth Surf. 122, 248–273. https://doi.org/10.1002/2016JF003973.

Whipple, K.X., Hancock, G.S., Anderson, R.S., 2000. River incision into bedrock: mechanics and relative efficacy of plucking, abrasion, and cavitation. Geology 112, 490–503. https://doi.org/10.1130/0016-7606(2000)112<490:RIIBMA>2.0.CO;2.

Whipple, K.X., Tucker, G.E., 1999. Dynamics of the stream-power river incision model: implications for height limits of mountain ranges, landscape response timescales, and research needs. J. Geophys. Res., Solid Earth 104, 17661–17674. https://doi.org/10.1029/1999JB900120.

Wobus, C., Whipple, K.X., Kirby, E., Snyder, N., Johnson, J., Spyropolou, K., Crosby, B., Sheehan, D., 2006. Tectonics from topography: procedures, promise, and pitfalls. In: Willett, S. (Ed.), Tectonics, Climate, and Landscape Evolution, Boulder, Colo., Geological Soc. of America. In: Geological Society of America Special Paper, vol. 398, pp. 55–74.

Wolf, S.G., Huismans, R.S., Braun, J., Yuan, X., 2022. Topography of mountain belts controlled by rheology and surface processes. Nature 606 (7914), 516–521. https://doi.org/10.1038/s41586-022-04700-6.

Xiao, X., White, E.P., Hooten, M.B., Durham, S.L., 2011. On the use of log-transformation vs. nonlinear regression for analyzing biological power laws. Ecology 92, 1887–1894. https://doi.org/10.1890/11-0538.1.

Zapata, S., et al., 2023. Drainage and sedimentary response of the Northern Andes and the Pebas system to Miocene strike-slip tectonics: a source to sink study of the Magdalena Basin. Basin Res. https://doi.org/10.1111/BRE.12769.